

Contents

5 Extracting Cross Sections	4
5.1 Overview	4
5.2 Electron Charge	7
5.3 Dead-Time	8
5.4 Targets	10
5.4.1 Cryo-Target Boiling Study	10
5.5 Detector Efficiencies	12
5.5.1 Trigger Efficiency	13
5.5.2 Vertical Drift Chamber Efficiency	15
5.5.3 Particle Identification Efficiencies	16
5.6 Monte Carlo Simulation	21
5.7 Cross Section Model	24
5.8 Event Selection and Corrections	25
5.8.1 Acceptance Correction	25
5.8.2 Central Momentum and Angle	27
5.8.3 Binning Correction	30
5.8.4 Cuts	30
5.9 From Yields to Cross Sections	31
5.10 Calculation of Errors	33
5.10.1 Statistical Errors	33

5.10.2 Systematic Errors	35
------------------------------------	----

Chapter 5

Extracting Cross Sections

5.1 Overview

Assuming the data is binned in the energy of scattered electrons, E' , the experimental raw cross section is usually written as:

$$\frac{d\sigma_{EX}^{raw}}{dE'd\Omega}(E_0, E'_i, \theta_0) = \frac{N_{EX}^i}{N_e \cdot N_{tg} \cdot \epsilon_{eff} \cdot (\Delta E'_{EX} \Delta \Omega_{EX})} \quad (5.1)$$

where the superscript i denotes the i th bin. E_0 is the initial energy which is fixed to 3.356 GeV in E08-014, E'_i is the scattered energy at the center of the bin, and θ_0 is the central scattering angle. $\Delta E'$ and $\Delta\Omega = \Delta\theta_{tg} \cdot \Delta\phi_{tg}$ are the momentum acceptance and the solid angle acceptance of the spectrometer; N_{EX}^i is the total number of scattered electron events; N_{tg} is the total number of scattering centers; N_e is the total accumulated electron charge from the beam; and ϵ_{eff} is the total efficiency of all detectors combined, including the detection efficiency, the cut efficiency and the electron-pion ratio after the PID cuts. In the rest of this chapter, the differential form of the cross section, $\frac{d\sigma}{dE'd\Omega}(E_0, E'_i, \theta_0)$, is abbreviated to $\sigma(E'_i, \theta_0)$.

The raw cross section in Eq (5.1) requires additional corrections to remove the effects from the spectrometer acceptance. Because E_0 and E'_i are altered when the

electron goes into and comes out from the target, the experimental cross section is usually called the radiated cross section and has to be further corrected by the radiative corrections. The final cross section is the born cross section, which can be directly compared with the theoretical calculations.

The basic procedure of extracting cross sections from experimental data is demonstrated in Fig. 5.1. First of all, the signals from detectors and electronics were stored in the raw data in the form of TDC channels, ADC channels and scaler counts. These signals have to be properly calibrated and converted into applicable quantities. The calibrated HRS optics matrix reconstructs the scattered electron's momentum, scattering angle and reaction point at the target plane. The full set of raw data was replayed with updated parameters in the data base. The calibration of detectors and the HRS optics matrices have been introduced in previous chapter.

Secondly, results of the beam charge monitor (BCM) calibration convert the BCM scaler counts into electron beam charge. The dead-time caused by the DAQ system is needed to be evaluated. N_{tg} is determined by the target thickness after the boiling study. Good electrons are identified by applying cuts on calibrated detector signals, and the efficiencies of the event selection can be individually evaluated. By binning the data with the kinematic variable, e.g. E' , in its proper acceptance range, one can extract the experiment yield in each bin. These procedures will be given in this chapter.

Meanwhile, the single arm Monte Carlo simulation (SAMC) generates simulation events with the same kinematic setting but with wider acceptance range to correct the acceptance effect of HRS. After weighting the simulation events with the cross sections calculated from models (e.g. XEMC in this experiment), the simulation yields were extracted with the same acceptance cuts and binning method. The Monte Carlo simulation and cross section models will also be discussed in this chapter.

Finally, the yield ratio method used to extract the cross sections will be introduced,

The flow-chart to extract inclusive cross sections

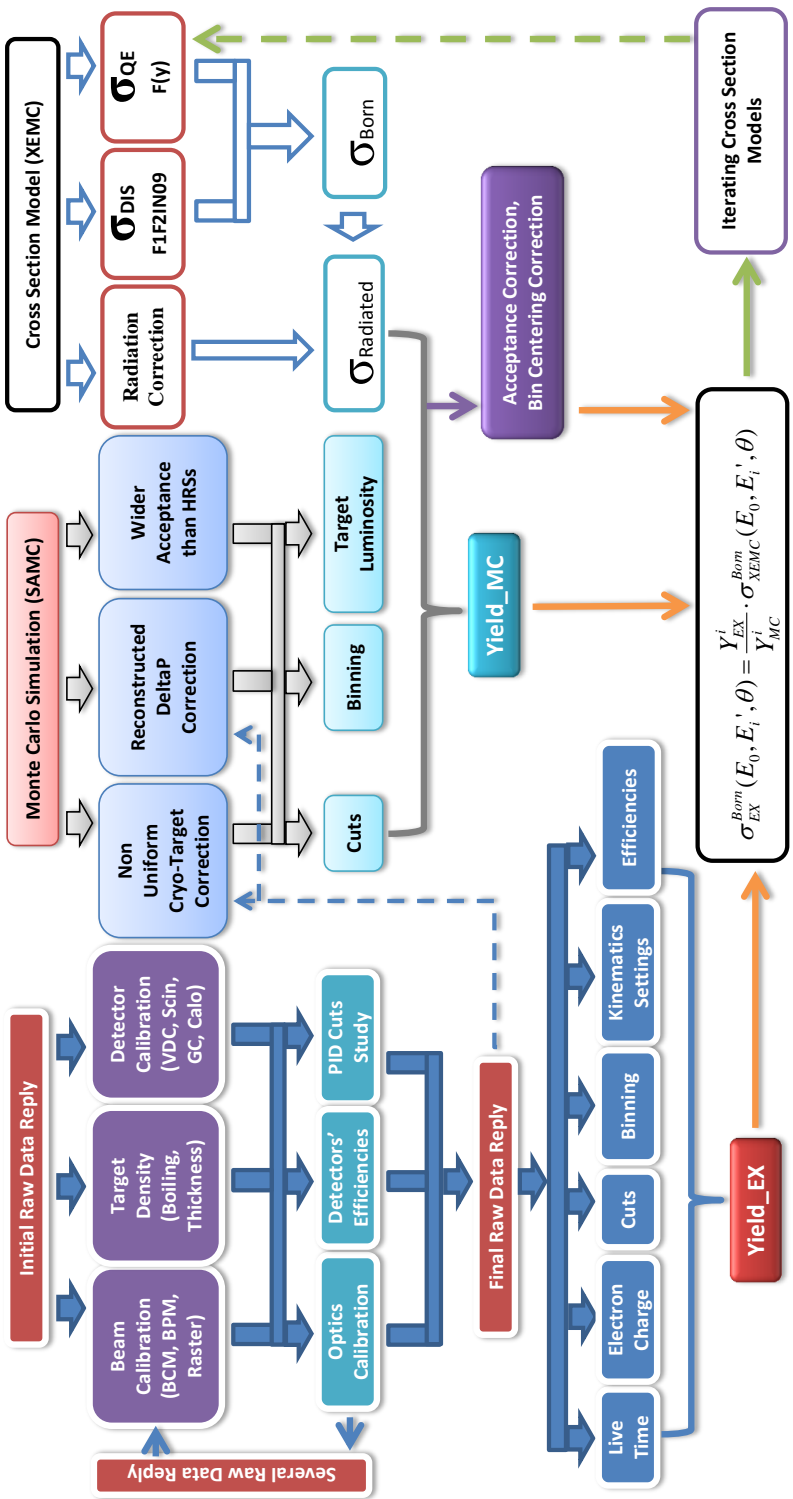


Figure 5.1: Flow-chart to extract cross section

followed by a discussion of errors.

5.2 Electron Charge

The accumulated electron charge from the beam was monitored by BCMs, the signals of which were recorded in scalers. The scalers signals, in term of number of counts, have been calibrated [3] to correctly reflect the accumulated electron charge. When the beam is stable during one run, the total electron charge is simply the product of the beam current and the total run time, and should be directly proportional to the total number of scaler counts. However, events taken during the beam trips are removed when the beam becomes unstable, hence the electron charge should be evaluated differently.

The average electron beam current in between two consecutive scaler events, called the real-time current, is calculated from the total electron charge collected between these events divided by the time gap. For example, between the i th and the $i + 1$ th event, the real-time current measured by the upstream BCM scaler, U_1 , is given by:

$$I_i^{U_1} = \Delta C_i^{U_1} / \Delta T_i, \quad (5.2)$$

where $\Delta C_i^{U_1} = C_{i+1}^{U_1} - C_i^{U_1}$ gives the charge accumulated between two scaler events with the time gap, $\Delta T_i = T_{i+1} - T_i$. Similarly, the real-time current measured by the downstream BCM scaler, D_1 , is also calculated. Other BCM scalers, U_3 and U_{10} (D_3 and D_{10}), which basically measure the same charge signal as U_1 (D_1) but with 3 times and 10 times amplification, respectively, were not involved in the calculation since the experiment used very high currents. The beam trip cut is applied on the average of the four real-time current values:

$$\frac{1}{2}(I_{i^*}^{U_1} + I_{i^*}^{D_1}) > I_{beam_trip_cut}. \quad (5.3)$$

where the cut value can be any value in between zero (when beam is tripped) and the value slightly below the maximum current. In this analysis, the beam trip cut is chosen to be 50% of the normal beam current.

The total electron charge after the beam trip cut is given as:

$$N_e = \frac{1}{2} \sum_{i^*} (\Delta C_{i^*}^{U_1} + \Delta C_{i^*}^{D_1}), \quad (5.4)$$

where i^* means summing over scaler events with beam current I_{i^*} higher than the cut.

After the data replay, scaler events are stored in the scaler trees, **RIGHT** for HRS-R and **LEFT** for HRS-L, respectively, and they are synchronized with trigger events in the **T** tree. There are certain number of trigger events recorded between two consecutive scaler events, and these events are assigned with the same beam current value when the real-time current between these two scaler events is evaluated. Consequentially, a beam trip cut removes all trigger events in between two scaler events if the real-time current is lower than the cut.

During the experiment, BCM scalers on HRS-L did not work properly. Due to the fact that the scalers on both HRSs record the same BCM signals, the real-time current for data taken in HRS-L is calculated using scaler events in HRS-R.

5.3 Dead-Time

Dead-time includes the electronic dead-time and the computer dead-time. The former refers to the situation when the coming trigger events are discarded when the front-end electronics of the DAQ system are processing the current trigger, and the later is due to the limitation of the computer speed which causes the loss of new events when the computer is writing the current event into the hard disk. Unless the computer is overloaded by processes other than the DAQ system, the computer dead-time is

negligible due to the usage of fast hard-drives. One evaluates the dead-time as the percentage of the trigger events being discarded to the total trigger events provided by detectors in a certain amount of time. The value of the dead-time directly depends on the performance of electronics and computers, but is also highly related to the total trigger rates. Other than increasing the performance of hardware, one typical method to reduce the dead-time is to control the total trigger rates below reasonable values by assigning a pre-scale factor to each trigger.

During data taking dead-time is monitored by using the electron dead-time monitor module (EDTM), which mixes pulse signals with fixed frequency into TDC signals from detectors. Since within a certain amount of time the total number of the pulse signals is known, the online dead-time value can be given by calculating the percentage of the pulse signals which are not recorded by the DAQ system. The value was usually controlled under 30% by changing the pre-scale factors before the start of the each run.

During the offline analysis, the average values of Dead-Time for the main production triggers were calculated individually for each run. Because scalers count all events from each trigger, while the total number of events recorded by the DAQ system were scaled by the pre-scale factor, the average dead-time value for the i th trigger is given by:

$$DT_{T_i} = 1 - \frac{PS_{T_i} \cdot N_{T_i}^{DAQ}}{N_{T_i}^{Scaler}}, \quad (5.5)$$

where $N_{T_i}^{Scaler}$ and $N_{T_i}^{DAQ}$ are the total number of scaler counts (in **RIGHT** for $i = 1$ or **LEFT** tree for $i = 3$) and trigger events (in **T** tree) in one run, respectively. PS_{T_i} is the pre-scale factor of the trigger. Events taken during the beam trip were removed since their rates were much lower than the normal rates.

A different quantity, live-time ($LT_{T_i} = 1 - DT_{T_i}$), is more commonly used in the data analysis. The total number of good events selected for data analysis should be

corrected by the live-time for each run:

$$N_{EX}^r = PS^r \cdot \frac{N_{recorded}^r}{LT^r}, \quad (5.6)$$

where $PS = PS1$ for HRS-R and $PS = PS3$ for HRS-L; r denotes the run number; N_{EX}^r and $N_{recorded}^r$ are the number of selected events which create triggers and the number of those events which are recorded by the DAQ system after pre-scaling, respectively. Note that without event selection, e.g., PID cuts, $N_{recorded}^r = N^{r,DAQ}$.

In this experiment, since only events from T_1 (T_3) were used for data analysis on HRS-R (HRS-L), the subscript, T_i , is omitted from any future discussion.

5.4 Targets

The total scattering center in Eq (5.1), or sometimes called the target luminosity, is calculated with known target thickness:

$$N_{tg} = \frac{\rho \cdot l \cdot N_a}{A}, \quad (5.7)$$

where ρ is the density of the target material in g/cm^3 , l is the effective target length in cm , N_a is the Avogadro's number and A is the nuclear number of the target.

5.4.1 Cryo-Target Boiling Study

When the electron beam is delivered to the target, the local temperature fluctuates and can cause the target density to vary with the beam current. Such a phenomena is called the boiling effect. While the density variation of solid targets is usually small, liquid and gas targets have significant boiling effects and their densities correlate to the beam current:

$$\rho_{cor} = \rho \cdot (1.0 - B \cdot I/100), \quad (5.8)$$

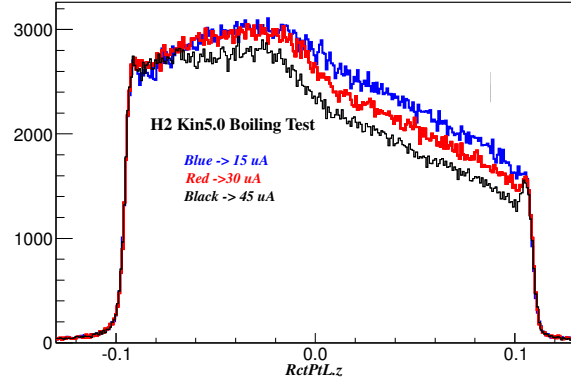
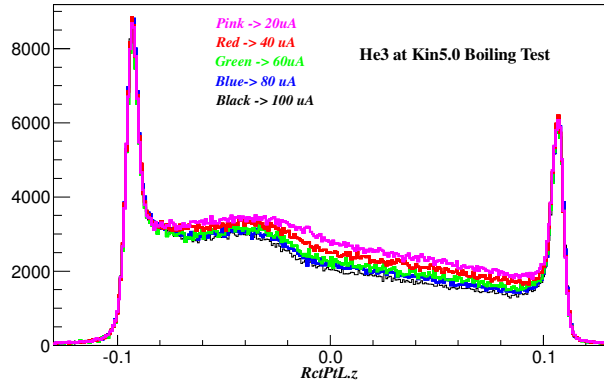
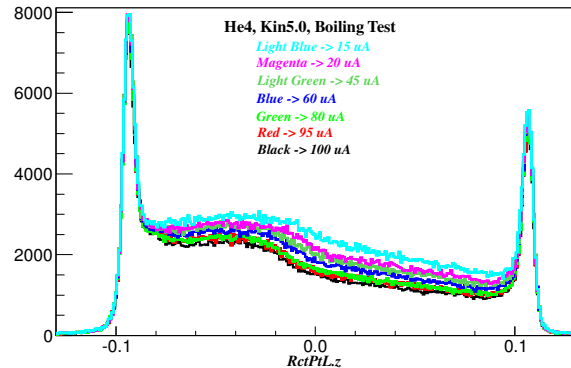
(a) 2H (b) 3He (c) 4He

Figure 5.2: Cryo-target bumps on z_{react} distributions due to the non-uniform density of long target. Three plots show the bump changing with beam current.

where I and B are the values of the beam current and the boiling factor for the target, respectively.

In E08-014, three cryogenic targets (cryo-targets), ^2H , ^3He and ^4He , are stored in 20 cm long aluminium cells. The design of the target flow resulted in a target density non-uniformly distributing along the target cell. When the beam is on, the boiling effect varied at different parts of the cell because the cooling flowed horizontally from upstream to downstream along the target. Fig. 5.2 shows the irregular density distribution and strong correlation between the density and the beam current. The luminosities of those cryo-targets can not be simply calculated from Eq (5.7).

A detailed treatment of these cryo-targets is discussed in Appendix D. A Monte Carlo simulation of the cryogenic target system demonstrated that the non-uniform distributions did not result from beam hitting other components in the target system. The boiling study was performed by dividing each target into several sections along the cell, where the boiling effect was individually evaluated. The relative density distribution of each target was extracted from the z_{react} distribution of the experimental data by using simulation data to remove the acceptance effect and the cross section effect. Since the target pressure and temperature were well maintained during the experiment, the absolute density should not deviate from the initial value in the installation report [7], and the small change was normalized by comparing the experimental yields to the simulation yields.

5.5 Detector Efficiencies

Every detector is designed to be sensitive to certain types of particles within the known energy ranges. However, due to the limitation of its performance, the detector is not necessarily able to measure all of such particles which pass through it. The percentage of particles being detected is called the detection efficiency (ϵ_{det}). Additionally, a certain number of good events are discarded during the data analysis by applying cuts on the detector's quantities. The percentage of good events remained after these

cuts is usually named the cut efficiency (ϵ_{cut}). In other words, the detection efficiency and the cut efficiency denote the survival rate of particles at the hardware level and at the software level, respectively. In this section, the efficiencies of the HRS detectors will be individually evaluated.

5.5.1 Trigger Efficiency

The traditional HRS production trigger is generated by the coincidence of logic signals from two scintillator planes (S1 and S2m), so the trigger efficiency is equal to the total detection efficiency of these two scintillators. The inefficiency rises when either S1 or S2m does not fire when a particle passes through. As discussed in Section 3.7, T2 (T4) is the trigger generated when only one of S1 and S2m signals coincide with the gas Cherenkov (GC) signal on HRS-R(-L). With the events from T2 (T4), one can calculate the trigger efficiency of T1 (T3), or equivalently T6 (T7) in E08-014, as follow:

$$\epsilon_{trigger_eff} = \frac{PS1(3) \cdot N_{T1(3)}}{PS1(3) \cdot N_{T1(3)} + PS2(4) \cdot N_{T2(4)}}, \quad (5.9)$$

where $N_{T1(2,3,4)}$ is number of events triggered by T1(2,3,4) and PS1(2,3,4) is the prescale factor of the trigger. Note that Eq. (5.9) is only valid when the GC has 100% detection efficiency. Events from T1 (T3) ($N_{T1(3)}$) may not be necessarily triggered by the GC, but events from T2 (T4) are recorded when the GC is fired, so $N_{T2(4)}$ has to be corrected by the detection efficiency of the GC. The trigger efficiency should be given by:

$$\epsilon_{trigger_eff} = \frac{PS1(3) \cdot N_{T1(3)}}{PS1(3) \cdot N_{T1(3)} + PS2(4) \cdot N_{T2(4)} / \epsilon_{det}^{GC}}, \quad (5.10)$$

where ϵ_{det}^{GC} is the detection efficiency of the GC. The HRS GCs usually have very high efficiency on detecting electrons so Eq. (5.9) is still valid. However, if the GC is inefficient the trigger efficiency has to be corrected by independently evaluating the

detection efficiency of the GC.

Since the design of T1 and T3 in E08-014 involves S1, S2m and the GC, events from T1 (T3) and T2(T4) are all triggered by requesting logic signals from the GC. The trigger efficiency does not depend on the detection efficiencies of the GC, which has been cancelled in Eq (5.9):

$$\epsilon_{trigger_eff} = \frac{PS1(3) \cdot N_{T1(3)}/\epsilon_{det}^{GC}}{PS1(3) \cdot N_{T1(3)}/\epsilon_{det}^{GC} + PS2(4) \cdot N_{T2(4)}/\epsilon_{det}^{GC}} = \frac{PS1(3) \cdot N_{T1(3)}}{PS1(3) \cdot N_{T1(3)} + PS2(4) \cdot N_{T2(4)}}. \quad (5.11)$$

In a word, the assumption that the trigger efficiency and the detection efficiency of S1 and S2m are equivalent is only valid when both T1 (T3) and T2 (T4) involve the logic signal from the GC.

The trigger efficiencies of T1 and T3 were calculated individually for each run, shown in Fig. 5.3. The results show that the triggers have very high efficiencies.

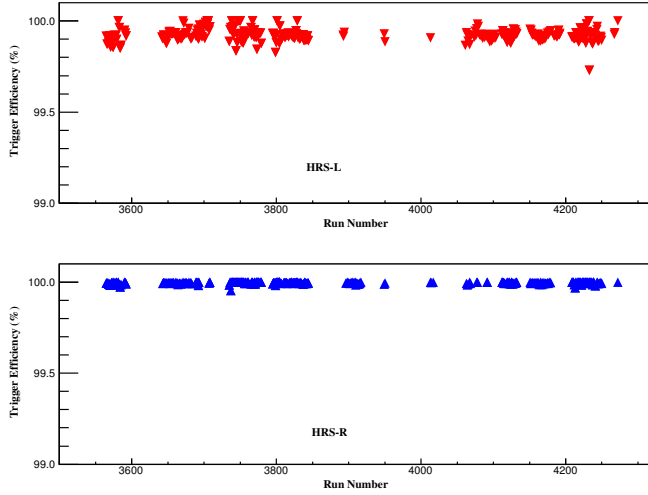


Figure 5.3: Trigger Efficiency vs Run Number, where the top plot is for T3 trigger on HRS-L and the bottom plot is for T1 trigger on HRS-R.

5.5.2 Vertical Drift Chamber Efficiency

The detection efficiency of vertical drift chambers (VDCs) is usually very high and any inefficiency is mainly caused by the mis-reconstruction of particle tracks given by the tracking algorithm. Only events with one track are kept for data analysis, and good events with zero-track and multi-tracks are discarded by applying a one-track-cut. The cut efficiency is generally called the one-track-cut efficiency, which is defined as:

$$\epsilon_{vdc} = \frac{N_{Track=1}}{N_{0 \leq Tracks \leq 4}}, \quad (5.12)$$

where $N_{Track=1}$ is the number of events with only one track and $N_{0 \leq Tracks \leq 4}$ is the number of events with tracks less than 4. Events with tracks more than 4 are extremely rare for HRS VDCs.

To correctly evaluate ϵ_{vdc} , good electrons were sampled by applying cuts on detector quantities. Any quantity that requires tracking information were avoided when selecting electrons, such as any quantity derived from VDCs, the acceptance cuts on the focal plane and the target plane quantities, and the energy sum of the calorimeter which requires the tracking information during the cluster reconstruction. Electrons can be alternately identified by cutting the calibrated ADC sum of the calorimeter and the GC's calibrated ADC sum. Events with multi-tracks can also be caused by multiple particles coming in one trigger window, and such events can be eliminated by requiring only one hit in each scintillator plane. Note that because paddles in S1 are overlapped, many good events coming through the overlapped region are discarded by applying such a cut, which should be avoided for any other part of data analysis.

Cosmic ray events usually come into the VDC with large angles and usually give bad tracking reconstruction, and they can be eliminated by cutting on the time-of-fly velocity (β_{TOF}) which is calculated from the timing quantities of S1 and S2m. However, the timing quantities of S1 and S2m was not calibrated in this experiment

due to the bad TDC signals, so cosmic ray events were not able to be removed. To reduce the effect from the cosmic ray background, data with high trigger rates, such as the carbon target data taken at the kinematic setting on the QE peak, were used to calculate the one-track-cut efficiency. From Table 5.1, the fraction of one-track and multi-track events are listed, where the one-track efficiency is mostly above 99%. The detection efficiency is the essential property of the detector and should not depend on the kinematic setting, hence one can conclude that the real value of the one-track-cut efficiency can be equal to the values calculated with data taken at high rates.

Number of tracks	0	1	2	3	4
HRS-L	0.0298%	99.1750%	0.7430%	0.0452%	0.0048%
HRS-R	0.0482%	99.3600%	0.5446%	0.0388%	0.0073%

Table 5.1: Fraction of different tracks events from quasi-elastic data,w/o β cut

5.5.3 Particle Identification Efficiencies

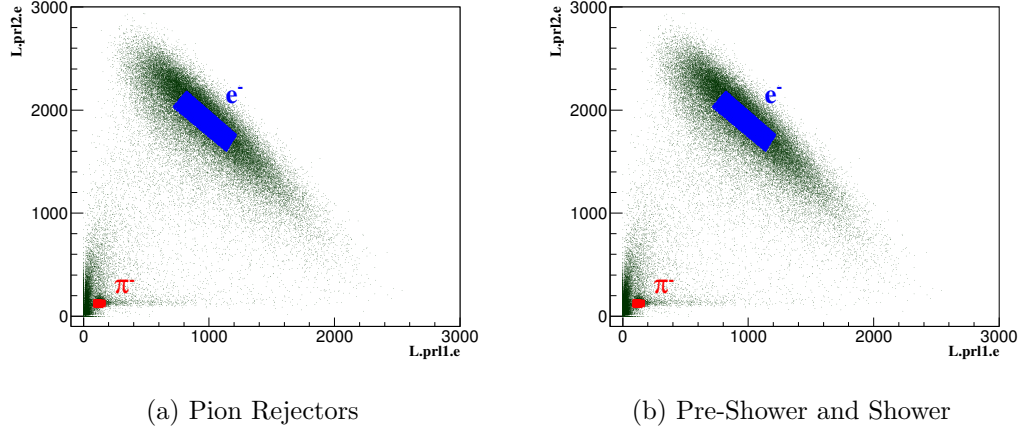


Figure 5.4: Electron (blue) and pion (red) samples from the calorimeters. In each plot, the x-axis and the y-axis are the total energies collected by the first layer and the second layer of the calorimeter, respectively. Electrons create large signals either in the first or the second layer during the cascade while the signals created by pions are relatively small in each layer. Graphic cuts were applied on these color regions to select the electrons and pions.

Electrons are identified by the GC and the calorimeter on each HRS. The GC

on each HRS give high detection efficiency, since the energy threshold of electrons to create Cherenkov radiation is only 18 MeV while pions and other heavy particles must have their energy above 4 GeV to fire the detectors. The efficiency is mainly related to the performance of mirrors in the detector to collect and focus the Cherenkov light.

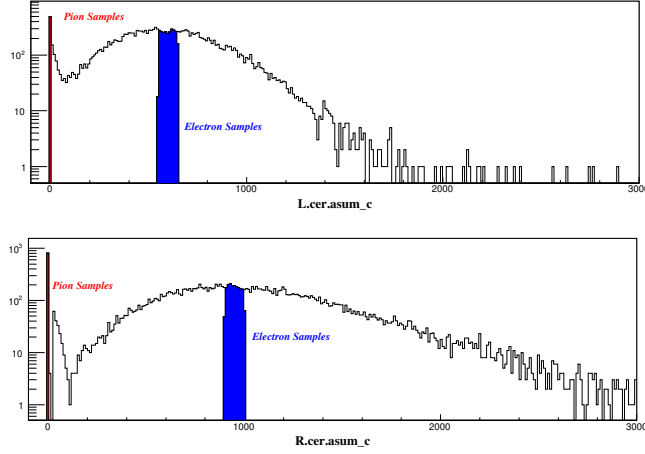


Figure 5.5: Electron and pion samples from the GC. Electrons were selected by applying cut on the main peak of the ten Cherenkov PMTs' ADC sum. Pions can not directly create Cherenkov light and they were selected by cutting on low ADC values since they leave very weak signals in the detector.

The detection efficiencies of the calorimeters are expected to be lower than the GCs. Each calorimeter is composed of many lead glass blocks, so the inefficiency arises when particles go through gaps in between blocks or hit the edges of the detector before it creates a shower.

During the offline analysis, the particle identification (PID) of electrons was performed by applying cuts on the calibrated quantities of the GC and the calorimeter. The cuts can reject most of unwanted particles, i.e., pions, and on the other hand, they may also accidentally discard good electrons. The PID study aims to obtain optimized PID cuts on the GC and the calorimeter, which can nearly eliminate pions while keeping as many electrons as possible. The cut efficiencies of the GC and the calorimeter have to be individually evaluated to correct the percentage of electrons

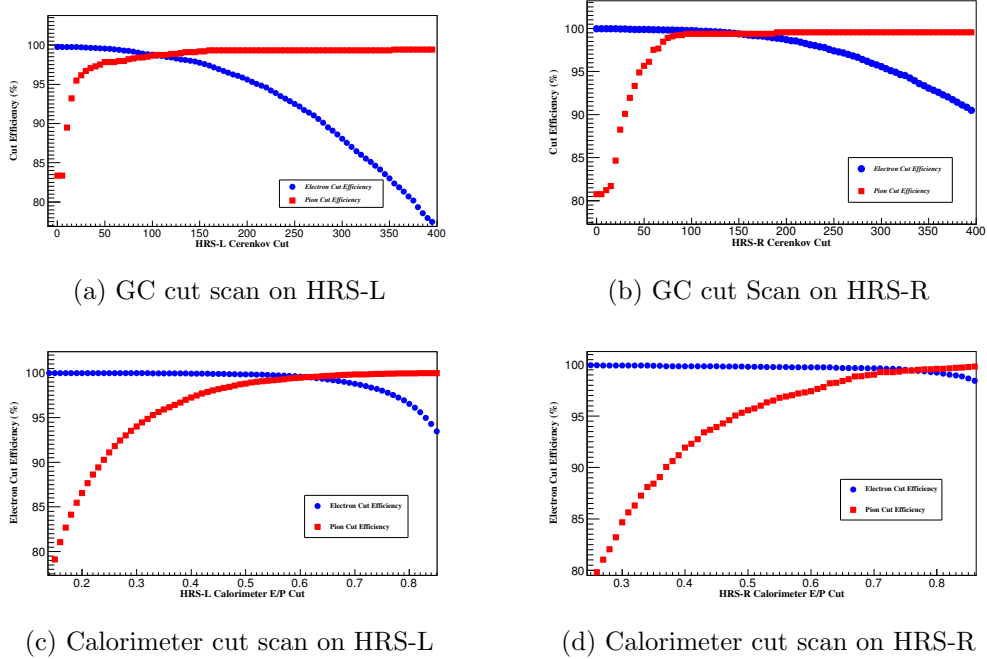


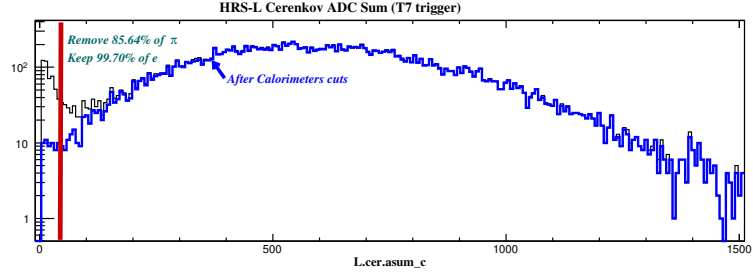
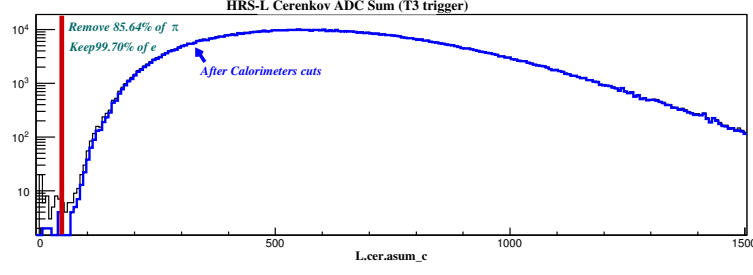
Figure 5.6: Cut scan of the GCs and the calorimeters on HRS-L (left) and HRS-R (right). The cut efficiencies of pion (red boxes) and electrons (blue dishes) were calculated with Eq. (5.13) and Eq. (5.14) by varying the cut on the GC or the calorimeter.

lost during the cuts.

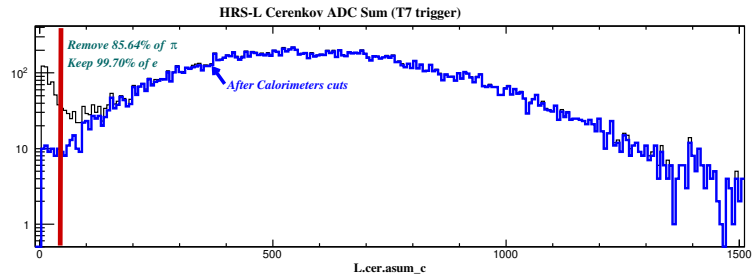
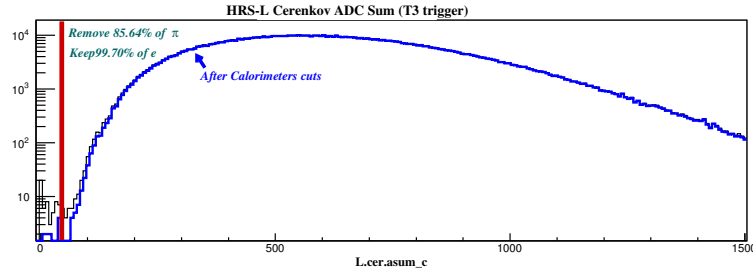
During the analysis of the GCs and the calorimeters, the detection efficiencies are usually evaluated together with the cut efficiencies based on the fact that one studies the detector with events which have already been detected.

In general, for experiments with a large pion background, extracting the ratio of the number of residual pions to the total number of electrons ($\epsilon_{\pi-e}$) is also very crucial. However, the pion production rate during E08-014 was very low compared with the electron rate in the QE region, and additionally, the new trigger design had already removed most of pions during online data taking by introducing the GC in the trigger system. Hence the value of $\epsilon_{\pi-e}$ is expected to be very small.

Events from the T6 and T7 triggers were used to study the PID cut efficiencies since they contain the most pions. The VDC one-track-cut and the acceptance cuts were applied to select good events. Then pure pion samples and pure electrons samples



(a) on HRS-L



(b) on HRS-R

Figure 5.7: PID cut on the GCs. In each panel, the top and bottom histograms plot the calibrated ADC sum of events triggered by T1 (T3) and T6 (T7) from HRS-R (HRS-L), respectively. Most of pions have already been rejected in events from T1 and T3 during data taking, so a minimum cut on the GC's ADC spectrum (≥ 50) can further remove rest of pions.

were chosen from the calorimeter (GC) when studying the cut efficiency of the GC (calorimeter). The **pion rejection efficiency** was defined as the percentages of pions

removed by applying the PID cuts:

$$\epsilon_{\pi-rej}^{GC(calо)} = \frac{N_{\pi}^{GC(calо)}}{N_{\pi-samples}^{calо(GC)}}, \quad (5.13)$$

and the electron cut efficiency can be calculated from:

$$\epsilon_{e-cut}^{GC(calо)} = \frac{N_e^{GC(calо)}}{N_{e-samples}^{calо(GC)}}, \quad (5.14)$$

where $N_{\pi-samples}^{calо(GC)}$ ($N_{e-samples}^{calо(GC)}$) is the pion (electron) samples from the calorimeter (GC) (Fig. 5.4 and Fig. 5.5). $N_{\pi}^{GC(calо)}$ is the number of pions rejected and $N_e^{GC(calо)}$ is the number of electrons left over after cutting on the GC (calorimeter), respectively. Note that the detection efficiency of the GC (calorimeter) has been absorbed in $\epsilon_{e-cut}^{GC(calо)}$ because electron samples from the calorimeter (GC) are not necessary to be detected by the GC (calorimeter).

As shown in Fig. 5.6, a cut scan was performed to study the distributions of the pion rejection efficiencies and the electron cut efficiencies by varying the cuts on the GCs and the calorimeters. Fig. 5.7a and Fig. 5.7b show that for the GC, the cut at the low value of the calibrated ADC sum, e.g., $L.cer.asum_c \geq 50$ for HRS-L or $R.cer.asum_c \geq 50$ for HRS-R, can already remove most of pions while keep more than 99% of electrons. The combined cuts on the calorimeter, $E/P \geq 0.5$ and $L.prl2.e \geq 100$ ($R.sh.e \geq 200$), can further remove more than 90% of pions while there is still more than 99% of electrons remaining (see Fig. 5.8a and Fig. 5.8b). In total, on HRS-L (HRS-R), 99.85% (99.62%) of pions are eliminated with these combined PID cuts, while 99.58% (99.86%) of electrons survives after the cuts. Considering the high electrons rates and low pion production for this experiment, one is not required to specially correct the pion contamination.

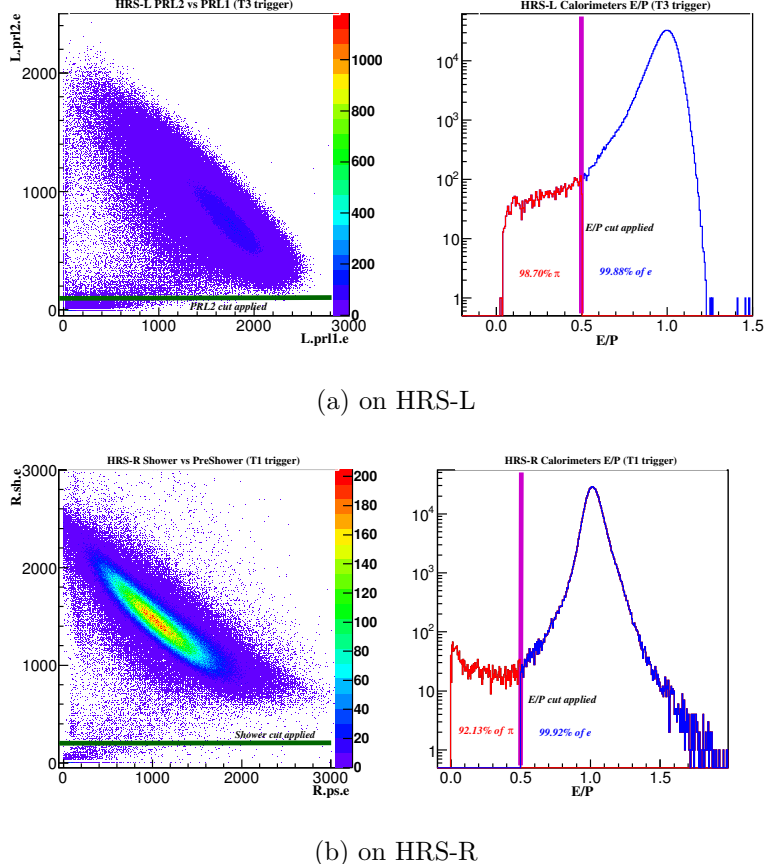


Figure 5.8: PID cut on the calorimeters. Most of pions can be removed by the E/P cut ($E/P \geq 0.5$) and the cut on the second layer’s ADC spectrum ($PRL2 \geq 100$ or $SH \geq 200$).

5.6 Monte Carlo Simulation

The Hall-A Single Arm Monte Carlo simulation tool (SAMC) is designed to simulate the transportation of particles from the target plane to the focal plane. SAMC was originally developed in FORTRAN [21] and then converted into C++ [22]. The electron beam position, the spectrometer settings, and the information of the target system can be specified in the code to match the experimental setting. A simulated event has its specified values of the incoming energy, the scattered momentum and the scattering angle, which are defined in the target coordinate system and called the target plane quantities. These quantities are randomly generated with uniform distributions, and with these quantities as inputs, each focal plane quantity is cal-

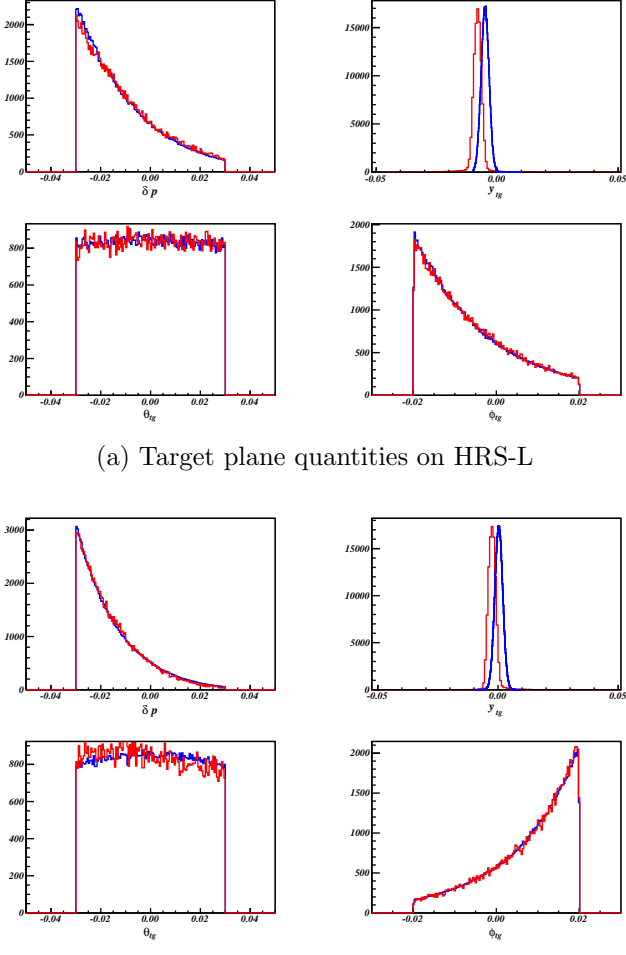
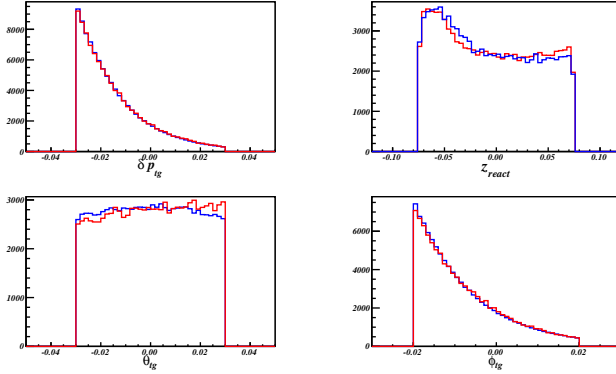
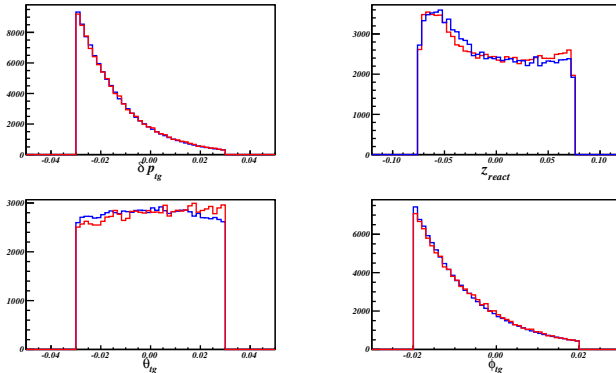


Figure 5.9: Simulation of ^{12}C target plane quantities, where red lines are simulation data from SAMC and blue lines are E08-014 data.

culated by a set of forward transportation functions which were generated by the SNAKE model [23]. After the focal plane quantities are smeared with the resolution of VDCs, a set of backward transportation functions is used to reconstruct the target plane quantities. During these two processes, events inside and outside the HRS acceptance can be individually identified. Before compared with the experimental data, the distributions of the target plane quantities and the focal quantities are weighted by the radiated cross section values of these simulated events which can be calculated using cross section models embedded in the code. In this analysis, a new cross section



(a) Target plane quantities on HRS-L



(b) Target plane quantities on HRS-R

Figure 5.10: Simulation of ${}^3\text{He}$ target plane quantities, where red lines are simulated data from SAMC and blue lines are the experimental data. The z_{react} distribution is simulated using the function fitted from data (Appendix D).

model and a special treatment to simulate the no-uniform cryogenic targets have been added in SAMC.

There were 20 million events generated for each target in each kinematic setting. Fig. 5.9 and Fig. 5.10 compare the distribution of reconstructed target plane quantities between simulated data and experimental data for ${}^{12}\text{C}$ and ${}^3\text{He}$, where the histograms for simulation data were weighted by the cross sections calculated by XEMC. The distribution of the same quantity from these two data sets agree nicely with each other. The distribution of z_{react} for the cryogenic target is simulated using the relative density distribution function extracted with the method discussed in Appendix D.

5.7 Cross Section Model

The inclusive electron scattering cross sections model used in this data analysis is XEMC, a C++ package to compute Born cross sections and radiated cross sections. A brief discussion of the cross section models and radiative correction is given in Appendix B.

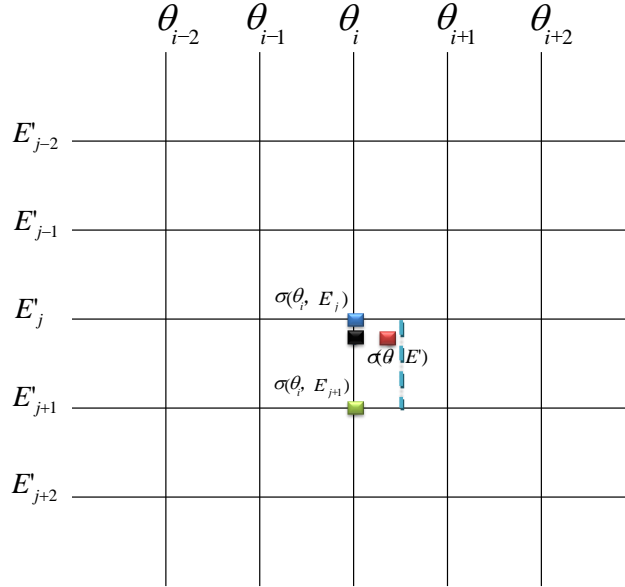


Figure 5.11: A sketch of cross section lookup tables. If $\theta_i \geq \theta < (\theta_i + \theta_{i+1})/2$, one sets $\sigma(\theta, E') \equiv \sigma(\theta_i, E')$, and vice versa. For $E'_j < E' < E'_{j+1}$, the cross section is calculated with the linear relationship given in Eq (5.15).

Calculating radiated cross section using XEMC takes several minutes for each event. To generate millions of simulated events, cross section look-up tables were generated for each target and kinematic setting. When generating each table, the ranges of scattering angle, $\Delta\theta$, and the scattered energy, $\Delta E'$, were slightly wider than the real HRS acceptance. Then $\Delta\theta$ was divided into 200 bins and $\Delta E'$ was also split into bins of 5 MeV. As shown in Fig. 5.11, the kinematic space for each setting is given as a 2-dimensional lattice where the born cross section and the radiated cross

section for each grid, (θ_i, E'_j) , are simultaneously calculated. Since the bin sizes are fine, for fixed momentum, the cross sections at different angle settings are considered to be equal within one θ bin, while for fixed angle, the cross section values are assumed to be proportional to the momentum values inside one E' bin. As illustrated in Fig. 5.11, for an given event, (θ, E') , the value of θ is replaced by the closest angle bin, for example, θ_i , and two momentum bins are specified so $E'_j < E' < E'_{j+1}$, so the cross section value for this event can be calculated using the linear relationship:

$$\sigma(E', \theta) = \sigma(E'_j, \theta^i) - \frac{E' - E'_j}{E'_{j+1} - E'_j} (\sigma(E'_j, \theta^i) - \sigma(E'_{j+1}, \theta^i)) \quad (5.15)$$

For the same event, the difference between the cross section obtained from the look-up table and the cross section directly calculated from XEMC is less than 0.1%, which indicates that the look-up tables works well. This method can dramatically reduce the computation time when generating simulation events.

5.8 Event Selection and Corrections

Events are distributed in the entire kinematic space within the acceptance of the HRSs. However, due to the statistical limitation, the kinematic space is divided by binning one or more kinematic variables and the cross section is evaluated at the center of each bin with events belong to this bin. The way to choose the acceptance range of the kinematic space and the binning method require additional corrections on the cross section. The electron events also have to be correctly selected by applying different cuts.

5.8.1 Acceptance Correction

The HRS acceptance includes both the range of momentum dispersion ($\Delta\delta p$) and the total solid angle which is composed of the out-of-plane angle (θ_{tg}) and the in-

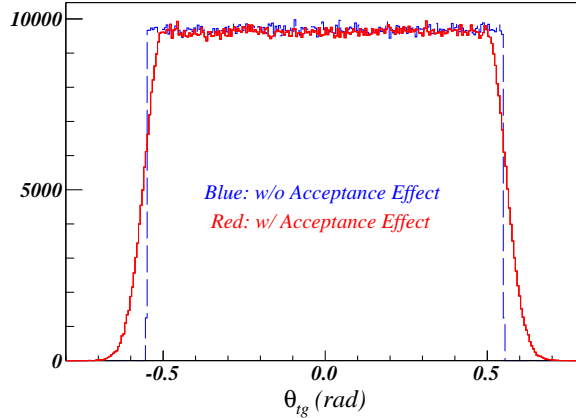


Figure 5.12: A demonstration of the acceptance effect, where the distribution of θ_{tg} is generated by assuming no any cross section weighting effect. The blue line shows that the acceptance is flat when the HRS acceptance is perfect, while the red line demonstrates the slowly fall-off of the acceptance edges. Such an effect is mainly due to the geometry of the HRS magnets and also contributed by the resolutions of the VDC tracking and the optics reconstruction. Green lines show the cuts to select the flat acceptance region.

plane-angle (ϕ_{tg}). For an extended target, the optics reconstructed reaction point along the beam direction (z_{react}) is also limited by the HRS acceptance. These four quantities, called the target plane quantities, are essential to reconstruct the reaction of the electron-scattering at the target. Due to the geometry of the HRS magnets, the event distributions of these quantities are not cut off immediately at the edge of the acceptance but instead, fall off relatively slowly with a gauss tail, as demonstrated in Fig. 5.12. Besides, the resolution of VDC tracking and the accuracy of the optics reconstruction can also smear the distributions of these quantities.

Choosing the right acceptance range of the target plane quantities is crucial in order to obtain the correct cross section results. Tight cuts on the target plane quantities were used to select events at the central region of the HRS acceptance, and the loose cuts on the edges of the focal plane variables can also remove these events which may have been multi-scattered inside the spectrometer. The acceptance cuts can be generally enlarged to increase the statistics of events in one bin, until the cross section results start to deviate from the results calculated using tighter cuts.

However, good events can be incorrectly discarded when one applies the combination cuts of the target plane quantities to define a valid acceptance region. Such an effect can be corrected by the HRS simulation for each bin:

$$A(E_0, E_i, \theta_0) = \frac{N_{MC}^{gen}}{\Delta E'_{MC} \Delta \Omega_{MC}} / \frac{N_{MC}^i}{\Delta E'_{bin} \Delta \Omega_{EX}}, \quad (5.16)$$

where $\Delta E'_{bin}$ are the bin size of E' which is fixed in both the simulated and experimental data, and $\Delta \Omega_{EX}$ is the selected angular acceptance range for the experimental data. N_{MC}^i is the number of simulation events in the i th bin, and it has to be applied with the same acceptance cuts as ones on the experimental events in the same bin, N_{EX}^i . N_{MC}^{gen} is the total number of simulated events without any cuts, which has been specified when generating these events. $\Delta E'_{MC}$ and $\Delta \Omega_{MC}$ define the full momentum and angular acceptance in the simulation, respectively, and they are slightly larger than the HRS acceptance. Overall, $\frac{N_{MC}^i}{\Delta E'_{bin} \Delta \Omega_{EX}}$ denotes the average number of events in the unit kinematic space which is limited by the HRS geometry, while the other term, $\frac{N_{MC}^{gen}}{\Delta E'_{MC} \Delta \Omega_{MC}}$, gives the average number of events in the unit kinematic space without any spectrometer limitations. Eq (5.16) usually refers to the acceptance correction.

5.8.2 Central Momentum and Angle

The kinematic space is determined not only by the acceptance of the HRS, but also by the central scattered momentum and the central scattering angle. The central momentum was given by the field values of the HRS magnets which were locked at the setting values by the HRS NMR system during the experiment. The off-line calculation gives the absolute value of the central momentum using the magnetic field of the dipole [1]:

$$P_0 = \sum_{i=0}^4 \gamma_i \cdot (10 \cdot B_{dipole}^{NMR})^i, \quad (5.17)$$

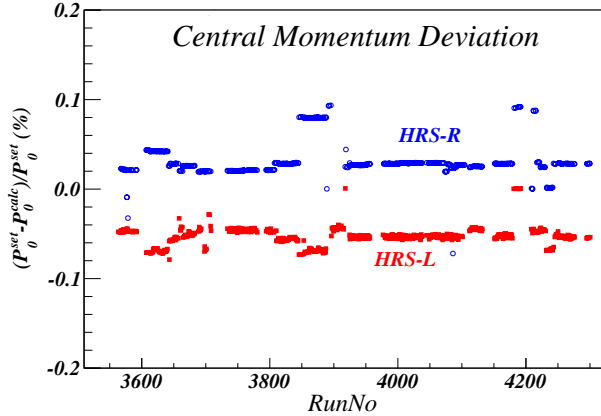


Figure 5.13: Central momentum deviation, where the blue circles and the red boxes are the deviation of the central momentum on HRS-R and HRS-L, respectively. The x-axis is the run number and the y-axis is the deviation in percentage.

where $\gamma_{1,2,3,4} = (0, 270.2, 0, -0.0016)$ for HRS-L and $\gamma_{1,2,3,4} = (0, 269.8, 0, -0.0016)$ for HRS-R. B_{dipole}^{NMR} is the field reading from the NMR monitor. Fig. 5.13 shows that the actually central momentum values were mostly off by $\pm 3\%$ while few of them were off by upto $\pm 10\%$. During the cross section extraction, the central momenta were assigned to the calculated values instead of the setting values.

The central scattering angle was specified during the experiment by moving the HRS to point at the angle marked on the floor and the value was stored in the EPICS data. These floor marks were drew with respect to the hall center and may not accurately reflect the true angle values. Moreover, the offsets between the spectrometer center and the hall center are different when the spectrometer points at different angles.

To obtain the actual central scattering angle each time when the spectrometer was moved, a survey was required to measure the offset between two center and to correct the errors of the floor marks. Unfortunately, the survey was not proceeded during this experiment and one had to use the survey reports from early experiments which had similar settings. Since the optics target was surveyed at the beginning of this experiment when the HRSs were set at 25° , the actual values of other angle settings

were corrected by identifying the difference between the optics target's central foil positions at 25° and at the other angle setting, Δz_{react} , as follow:

$$\theta_{tg} = \frac{D_x + x_{sieve} - y_{beam}}{L - x_{beam} \cdot \sin\theta_0^{set} - \Delta z_{react} \cdot \cos\theta_0^{set}}, \quad (5.18)$$

$$\phi_{tg} = \frac{D_y + y_{sieve} - x_{beam} \cdot \cos\theta_0^{set} + \Delta z_{react} \cdot \sin\theta_0^{set}}{L - x_{beam} \cdot \sin\theta_0^{set} - \Delta z_{react} \cdot \cos\theta_0^{set}}, \quad (5.19)$$

$$\theta_0^{true} = \arccos \left(\frac{\cos\theta_0^{set} - \phi_{tg} \sin\theta_0^{set}}{\sqrt{1 + \theta_{tg}^2 + \phi_{tg}^2}} \right), \quad (5.20)$$

where D_x , D_y , x_{sieve} , y_{sieve} and L are given in Table ?? and Table ???. The beam position (x_{beam} , y_{beam}) was locked at (-2.668 mm, 3.022 mm) during the experiment. θ_0^{set} is the central scattering reading from the floor marks and θ_0^{true} is the actual central scattering angle after the correction. As shown in Table ??, the calculation showed that the maximum offset between θ_0^{true} and θ_0^{set} was not larger than 0.04° . The value of θ_0^{true} was calculated for runs taken at each run period when the spectrometer was moved to different positions. The cross sections were calculated with these updated values.

RunNo	$\theta_0^{set}(L)$	$\theta_0^{true}(L)$	$\theta_0^{set}(R)$	$\theta_0^{true}(R)$
3565~3656	25.00	25.00	25.00	25.00
3657~3683	21.00	21.03	21.00	21.04
3684~3708	23.00	23.00	23.00	23.01
3735~3891	25.00	24.99	25.00	25.00
3892~3916	—	—	21.00	21.03
3917~4071	28.00	27.98	28.00	27.99
4073~4103	21.00	21.04	28.00	27.99
4112~4179	23.00	23.00	23.00	23.04
4181~4241	25.00	24.98	25.00	25.00
4242~4250	21.00	21.02	21.00	21.03
4251~4299	28.00	27.98	28.00	27.99

Table 5.2: E' binning size and range

5.8.3 Binning Correction

The cross section results are calculated by binning the data on E' . The range and step size of binning is given in the following table:

Kin	3.1	3.2	4.1	4.2	5.0	5.05	5.1	5.2	6.5
E'^{Min}	2.76	2.90	2.71	2.88	2.38	2.52	2.66	2.85	2.70
E'^{Max}	3.05	3.21	3.00	3.19	2.63	2.78	2.94	3.14	2.99
$\Delta E'$	0.01	0.01	0.01	0.01	0.01	0.01	0.01	0.01	0.01

Table 5.3: E' binning size and range

From Eq (5.1), when binning on E' the cross section in each bin is given as a function of the central scattering angle (θ_0) and the momentum value at the center of the bin (E'_i). However, events in each bin carry different momenta varying from $E'_i - \frac{1}{2}\Delta E'$ to $E'_i + \frac{1}{2}\Delta E'$, while their central scattering angles can deviate from θ_0 within the solid angle, $\Delta\Omega_{EX}$. To correct the effect, a **bin-centering correction** is calculated using the simulation data and the cross section model:

$$B(E_0, E_i, \theta_0) = \frac{\sigma_{XEMC}^{rad}(E_0, E'_i, \theta_0)}{\sum_{j \in i} \sigma_{XEMC}^{rad}(E_0, E'_j, \theta_j)}, \quad (5.21)$$

where $\sum_{j \in i}$ means summation over the radiated cross section values, $\sigma(E'_j, \theta_j)$, of all Monte Carlo events in the i th x_{bj} bin. $\sigma_{XEMC}^{rad}(E'_i, \theta_0)$ and $\sigma_{XEMC}^{rad}(E'_j, \theta_j)$ are calculated from the XEMC model.

5.8.4 Cuts

In addition to cutting on the binning variable, there are several other cuts which were applied to select good scattered electron events/ For example, in HRS-L:

1. Cut on production trigger events (see Appendix A), $DBB.evtypebits >> 3 \& 1$ ("3" is replaced by "1" for HRS-R);
2. Remove pulser events generated by EDTM modules, $DBB.edptl[0] == 0$;

3. Beam trip cut, $left_current >= I_{trip}$;
4. Select events with only one track in VDCs, $L.tr.n == 1$;
5. Cuts on the focal plane acceptance, $|x_{fp}| <= 0.75 \&\& |y_{fp}| <= 0.55 \&\& |\theta_{fp}| <= 0.15 \&\& |\phi_{fp}| <= 0.045$;
6. Cuts on the target plane acceptance, $|\delta p_{tg}| <= 0.03 \&\& |ReactPointZ| <= 0.07 \&\& |\theta_{tg}| <= 0.03 \&\& |\phi_{tg}| <= 0.02$;
7. PID cuts on the GC and the calorimeter, $L.cer.asum_c >= 50 \&\& epL <= 0.5 \&\& L.prl2.e <= 100$, where epL denotes the energy sum of the calorimeter divided by the central momentum (E/P).

For a list of runs, the total number of events after the cuts defined above is given by:

$$N_{EX}^i = \sum_r \frac{PS_{T_i}^r \cdot N_{T_i}^r}{LT_{T_i}^r}, \quad (5.22)$$

where T_i defines the type of trigger we are interested in, r represents one of runs in the list, $PS_{T_i}^r$ is the pre-scale factor of this trigger, and $N_{T_i}^r$ is the total number of events from T_i and recorded by DAQ after cutting out beam trip. Notes that events from each run are individually corrected by the Live-Time ($LT_{T_i}^r$) before they are added together.

5.9 From Yields to Cross Sections

The experimental Born cross section can be calculated from Eq (5.1) after applying the acceptance correction (Eq (5.16)) and the bin-centering correction (Eq (5.21)):

$$\sigma_{EX}^{Born}(E_0, E'_i, \theta_0) = A(E_0, E'_i, \theta_0) \cdot B(E_0, E'_i, \theta_0) \cdot \sigma_{EX}^{rad}(E_0, E'_i, \theta_0) \cdot RC(E_0, E'_i, \theta_0) \quad (5.23)$$

Note that the initial electron energy, E_0 , is fixed at 3.356 GeV during this experiment. The last term is the radiation correction factor:

$$RC(E_0, E'_i, \theta_0) = \frac{\sigma_{XEMC}^{Born}(E_0, E'_i, \theta_0)}{\sigma_{XEMC}^{rad}(E_0, E'_i, \theta_0)}. \quad (5.24)$$

Extraction of cross sections from Eq 5.23 largely relies on the performance of the simulation and the cross section model, which, however, can not be directly examined from the cross section results. Two useful quantities, the experimental yield and the Monte Carlo (MC) yield, can be extracted to directly compare their difference. The experimental yield can be written as:

$$Y_{EX}^i = \frac{N_{EX}^i}{N_e \cdot \epsilon_{eff}}, \quad (5.25)$$

and the MC yield is given by:

$$Y_{MC}^i = N_{tg} \cdot \sum_{j \in i} \sigma_{model}^{rad}(E_0, E'_j, \theta_j) \cdot \frac{\Delta\Omega_{MC} \Delta E'_{MC}}{N_{MC}^{gen}}. \quad (5.26)$$

The ratio of the experimental yield to the MC yield should be close to one if the performance of the HRS can be well simulated by the MC data and the XEMC model produces cross sections relatively close to the real results. The experimental Born cross section from Eq 5.23 can be rewritten as:

$$\sigma_{EX}^{Born}(E_0, E'_i, \theta_0) = \frac{Y_{EX}^i}{Y_{MC}^i} \cdot \sigma_{XEMC}^{Born}(E_0, E'_i, \theta_0), \quad (5.27)$$

The yield ratio method can largely reduce the bias caused by the choice of different cross section models. While the experimental yield is completely extracted from the data and remains unchanged, one can iterate the cross section model and apply necessary corrections only on the MC yield until the the yield ratio becomes close

to one for different E' bins. Furthermore, the acceptance cuts on the HRS can also be studied by varying the cuts and checking the distribution of the yield ratio as a function of the binning variable. Most of other potential issues, such as bad data, incorrect input parameters and so on, can also be examined in the yield ratio method.

5.10 Calculation of Errors

One of most important tasks to extract experimental cross sections is to calculate the errors which includes both systematic errors and the statistical errors. Systematic errors are introduced by the experimental instrumentation, the simulation tool and the cross section model, etc. Statistical errors relate to the number of measurements on one quantity during the experiment. It is very important to properly propagate the errors when extracting new quantities from the existing quantities and any mistakes such as mis-counting or multi-counting should be avoided during the cross section extraction. The detailed explanation of the error calculation and propagation is given as follows.

5.10.1 Statistical Errors

The detail propagation of Statistical Errors is discussed bellow:

1. N_e : From Eq.5.4, since the charge is obtained from the average of two BCM monitor outputs (U_1 and D_1), the error is also averaged:

$$\delta N_e^r = \sqrt{\frac{(\delta N_e^{r,D_1})^2 + (\delta N_e^{r,U_1})^2}{2}} = \sqrt{\frac{N_e^{r,D_1} + N_e^{r,U_1}}{2}} = \sqrt{\frac{N_e^r}{2}}, \quad (5.28)$$

where, r means the run number. Hence,

$$\delta N_e = \sqrt{\sum_r (\delta N_e^r)^2} = \sqrt{\frac{\sum_r N_e^r}{2}} = \sqrt{\frac{N_e}{2}}. \quad (5.29)$$

2. **Live-Time:** Form Eq.5.6, when $PS^r = 1$:

$$\delta LT^r = LT^r \cdot \sqrt{\frac{1}{N^{r,Scaler}} + \frac{1}{N^{r,DAQ}}}, \quad (5.30)$$

where $PS = PS1$ for HRS-R and $PS = PS3$ for HRS-L. When $PS^r > 1$, the calculation of δLT^r is given differently [24]:

$$\delta LT^r = LT^r \cdot \sqrt{\frac{1}{N^{r,Scaler}} - \frac{1}{N^{r,DAQ}}}. \quad (5.31)$$

3. N_{EX} : From Eq.5.22 and $N_{EX} = \sum_r N_{EX}^r$ for all runs, we have:

$$\delta N_{EX}^r = N_{EX}^r \cdot \sqrt{\frac{1}{N_{recorded}^r} + \left(\frac{\delta LT^r}{LT^r}\right)^2}, \quad \delta N_{EX} = \sqrt{\sum_r (\delta N_{EX}^r)^2}, \quad (5.32)$$

where $N_{recorded}^r$ is defined in Eq (5.6).

4. Y_{EX} : From Eq.5.25,

$$\delta Y_{EX} = Y_{EX} \cdot \sqrt{\left(\frac{\delta N_{EX}}{N_{EX}}\right)^2 + \left(\frac{\delta N_e}{N_e}\right)^2 + \left(\frac{\delta \epsilon_{eff}}{\epsilon_{eff}}\right)^2}, \quad (5.33)$$

where ϵ_{eff} is set to one and its statistic error and systematic error are set to zero and 1%, respectively.

5. Y_{MC} : From Eq.5.26,

$$\delta Y_{MC} = Y_{MC} \cdot \sqrt{\left(\frac{\delta \sum_{j \in i}}{\sum_{j \in i}}\right)^2 + \left(\frac{\delta N_{MC}^{gen}}{N_{MC}^{gen}}\right)^2}, \quad (5.34)$$

where $\delta \sum_{j \in i} = \sum_{j \in i} \cdot \frac{1}{\sqrt{N_{MC}^i}}$, since it is summarizing the cross section values of MC events (N_{MC}^i) in one bin.

6. σ_{EX}^{Born} : From Eq.5.27,

$$\delta\sigma_{EX}^{Born} = \sigma_{EX}^{Born} \cdot \sqrt{\left(\frac{\delta Y_{EX}}{Y_{EX}}\right)^2 + \left(\frac{\delta Y_{MC}}{Y_{MC}}\right)^2} \quad (5.35)$$

5.10.2 Systematic Errors

The entire list of systematic errors has not been determined in this thesis. Few items are given as follows:

1. N_{tg} : Form Eq (5.7) and Eq (5.8), there are three terms that can introduce errors: beam current measurement and calculation (δI), accuracy of Boiling Factors (δB), and the accuracy of target thickness measurement ($\delta \rho$). First two terms were temporarily set to zero. Hence:

$$\delta N_{tg} = \frac{\delta \rho}{\rho} \cdot N_{tg} \quad (5.36)$$

2. $N_{efficiency}$: 1% systematic errors is assigned to each of VDC One-Track efficiency, trigger efficiency, detection and cut efficiencies of Gas Cherenkov and Calorimeters.

3. **Optics:**

4. **δp correction (HRS-R only):**

5. **Radiation correction:**

Bibliography

- [1] J. Alcorn *et al.*, Nucl. Instrum. Meth. **A522**, 294 (2004).
- [2] B. Reitz, Hall-A BPM Calibration Procedure, <http://hallaweb.jlab.org/podd/doc/bpm.html>.
- [3] P. Solvignon-Slifer, E08-014 BCM calibration report, 2012.
- [4] P. V. J. Berthot, Nucl. Phys. News **9**, 12 (1990).
- [5] O. Ravel, 1997.
- [6] Jefferson lab cryogenic group, wwwold.jlab.org/eng/cryo.
- [7] D. Meekins, E08-014 target report, http://hallaweb.jlab.org/experiment/E08-014/analysis/HallA_Target_Configuration_Apr2011.pdf, 2011.
- [8] R. Bock and A. Vasilescu, The Particle Detector Brief ook.
- [9] E. Jastrzembski, 1997.
- [10] ROOT/C++ Analyzer for Hall A.
- [11] ROOT - A Data Analysis Framework by CERN, <http://root.cern.ch/drupal/>.
- [12] E08-014 Harp scan results, 2011.
- [13] A. Ketikyan *et al.*, About Shower Detector Software, 1997.
- [14] H. Lu *et al.*, Shower Calibration and Efficiency for E97-110, ShowerCalibrationandEfficiencyforE97-110, http://hallaweb.jlab.org/experiment/E97-110/tech/shower_calib.ps.gz", 2005.
- [15] N. Liyanage, Optics Calibration of the Hall A High Resolution Spectrometers using the new optimizer, <http://hallaweb.jlab.org/publications/Technotes/files/2002/02-012.pdf>, 2002.
- [16] Hall A survey report 1343, <http://www.jlab.org/eng/survalign/documents/dthalla/A1343.pdf>, 2010.

- [17] Hall A survey report A1249, <http://www.jlab.org/eng/survalign/documents/dthalla/A1239.pdf>, 2009.
- [18] Hall A survey report A1239, <http://www.jlab.org/eng/survalign/documents/dthalla/A1249.pdf>, 2009.
- [19] G. Jin, Measurement of the Target Single-Spin Asymmetry in Quasi-Elastic ^3He , 2011.
- [20] J. Huang, HRS Optics Optimizer, 2009.
- [21] A. Duer, Single Arm Monte Carlo for Polarized ^3He experiments in Hall A v.0.2, <http://hallaweb.jlab.org/publications/Technotes/files/2001/01-004.pdf>, 2002.
- [22] H. Yao, Ph.D Thesis, Temple University , 2011.
- [23] J. LeRose, HRS transportation functions.
- [24] V. Sulkosky, Ph.D Thesis, College of William and Mary, 2007.
- [25] G. B. West, Physics Reports **18**, 263 (1975).
- [26] C. Ciofi degli Atti, S. Liuti, and S. Simula, Phys. Rev. C **41**, R2474 (1990).
- [27] S. Boffi, C. Giusti, and F. Pacati, Physics Reports **226**, 1 (1993).
- [28] J. Arrington, Inclusive Electron Scattering From Nuclei at $x \gtrsim 1$ and High Q^2 , 1998.
- [29] P. Bosted and V. Mamyan, Empirical Fit to electron-nucleus scattering, 2012, arXive 1203.2262.
- [30] N. Fomin, Ph.D Thesis, University of Virginia, 2008.
- [31] A. Daniel, Ph.D Thesis, Houston University, 2007.
- [32] R. D. McKeown, Phys. Rev. Lett. **56**, 1452 (1986).
- [33] J. S. O'Connell *et al.*, Phys. Rev. C **35**, 1063 (1987).
- [34] J. Bevelacqua, FIZIKA **1**, 129 (1992).
- [35] J. W. Lightbody and J. S. O'Connell, Comput. Phys. **2**, 57 (1988).
- [36] K. Slifer, Ph.D Thesis, Temple University , 2003.
- [37] W. Armstrong, InSane - QFS model, http://quarks.temple.edu/~whit/code/InSANE++/html/da/dfc/group__xsections.html.
- [38] P. E. Bosted and M. E. Christy, Phys. Rev. C **77**, 065206 (2008).

- [39] L. W. Mo and Y. S. Tsai, Rev. Mod. Phys. **41**, 205 (1969).
- [40] S. Stein *et al.*, Phys. Rev. D **12**, 1884 (1975).
- [41] O. Benhar, D. Day, and I. Sick, Rev. Mod. Phys. **80**, 189 (2008).
- [42] S. Covrig, E08-014 Cryogenic Target System Simulation, 2013.
- [43] L. L. Frankfurt, M. I. Strikman, D. B. Day, and M. Sargsyan, Phys. Rev. C **48**, 2451 (1993).
- [44] CLAS Collaboration, K. S. Egiyan *et al.*, Phys. Rev. Lett. **96**, 082501 (2006).
- [45] N. Fomin *et al.*, Phys. Rev. Lett. **108**, 092502 (2012).